Journal of
Materials Chemistry C

PAPER

View Article Online
View Journal | View Issue

Cite this: *J. Mater. Chem. C*, 2026, **14**, 3994

Excited-state dynamics of colloidal gold nanoshells functionalized with trimethoxysilylazachalcones

Marta Gordel-Wójcik, *[abe] Muhammed A. Thottappali, [b] Marek Pietrzak,[c]
Elizaveta F. Petrusevich, [d] Jiří Vohlídal, [e] Jiří Pfleger [b] and
Beata Jędrzejewska [c]

Received 4th October 2025,
Accepted 6th January 2026

DOI: 10.1039/d5tc03618f

rsc.li/materials-c

In this study, we present a new synthetic approach to obtain trimethoxysilylazachalcones, a family of donor–acceptor chromophores exhibiting strong intramolecular charge-transfer behavior. Their distinct optical features, validated through comprehensive spectroscopic analysis and theoretical modeling, make them promising candidates for advanced functional applications. To harness and further enhance their photophysical potential, the chromophores were covalently anchored onto plasmonic gold nanoshells (NSs), forming hybrid nanostructures engineered for enhancing excited state processes through plasmon–molecule interactions. Femtosecond transient absorption spectroscopy revealed pronounced differences in the excited-state dynamics between the free and hybrid systems. While several plasmon-related processes, such as local electromagnetic-field enhancement, hot-electron transfer to the molecular LUMO, and the suppression of non-radiative decay through restricted molecular mobility and strong interfacial electronic coupling-are possible, we believe that the dominant contribution in our measurements arises from nanoparticle heating and its resulting thermal response. The results underscore the potential of such plasmon-enhanced hybrid materials in technologies where control over excited-state dynamics is essential. Applications span photonic devices, optical sensors, and light-triggered biomedical tools such as photodynamic therapy and high-resolution bioimaging, where prolonged excited-state lifetimes can directly translate into improved functionality and sensitivity.

Introduction

Chalcones are a class of compounds whose molecules contain a conjugated sequence of two aromatic rings, A and B, connected by a (prop-1-en-3-oxo)-1,3-diyl group (so-called ketoethylene): A–CO–CH=CH–B (Fig. 1).

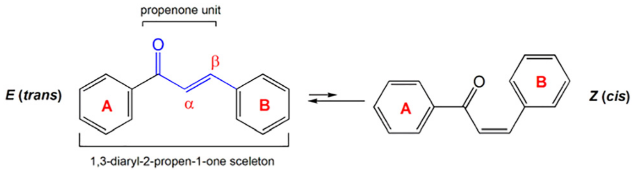

Fig. 1 Structures of *E* (*trans*) and *Z* (*cis*) isomers of chalcones.

They are also called open-chain flavonoids and considered to be their biosynthetic precursors.[1] In addition to chalcone with a three-carbon alkenone unit, some saturated ketones with a three-carbon alkanone unit, often referred to as dihydrochalcones, belong to this class of organic compounds. The presence of a double bond in the chemical skeleton of chalcone, *i.e.* 1,3-diaryl-2-propen-1-one, causes this molecule to exist as *E* and *Z* isomers, with the *Z* isomer being thermodynamically more unstable[2,3] due to steric effects of ring A with carbonyl group in this conformer.[4]

In the nature, chalcones occur most often as crystalline solids that can be found in stems, roots, flowers, fruits and leaves of various plants.[4] They contain mainly hydroxyl substituents, but also alkoxy, alkyl and additional cyclic groups. In addition, they can occur as dihydrochalcones, dimers (bichalcones) and glycosides.

---

[a] *Faculty of Chemistry, University of Wrocław, 14.p F. Joliot-Curie Street, 50-383, Wrocław, Poland. E-mail: marta.gordel-wojcik@uwr.edu.pl*
[b] *Department of Polymers for Electronics and Photonics, Institute of Macromolecular Chemistry, Czech Academy of Sciences, Heyrovského nám. 2, 16206 Prague 6, Czech Republic*
[c] *Faculty of Chemical Technology and Engineering, Bydgoszcz University of Science and Technology, Seminaryjna 3, 85-326 Bydgoszcz, Poland*
[d] *Faculty of Chemistry, University of Gdańsk, Fahrenheit Union of Universities in Gdańsk, Wita Stwosza 63, 80-308 Gdańsk, Poland*
[e] *Department of Physical and Macromolecular Chemistry, Faculty of Science, Charles University, Prague, Czech Republic*

The presence of the reactive propenal-1,3-diyl group (–CO–CH═CH–) makes chalcones biologically active compounds;[2,5] with a wide range of applications in pharmacology and medicine.[3,6] The conjugation of the β–unsaturated bond with the carbonyl group is considered to be the center determining the biological activity of chalcones, without which this compound would partially or completely lose the ability to demonstrate any biological significance.[7] Plants containing chalcones such as pepper, licorice, angelica, and butcher's broom have been used in Asia, Africa, and South America as anti-inflammatory and antiviral agents. The antioxidant properties of chalcones in fruits and vegetables are also known. Synthetic chalcones are widely used in various applications in biological and material sciences due to their small molecular size, convenient and inexpensive synthesis, flexibility in structural modification, and being a useful building block for a wide range of heterocyclic compounds.[8,9] In addition to their pharmacological and medical applications such as anti-cancer, anti-ulcer, anti-tuberculosis, anti-inflammatory, antibacterial, antiviral, antiparasitic, antidiabetic, and antioxidant activities,[8–10] they also play a significant role in material sciences. Beyond their biological activity, chalcones and their derivatives have attracted considerable attention in materials science. Owing to their conjugated π-electron systems and tunable donor–acceptor architectures, they have been explored as functional components in nonlinear optical (NLO) materials,[11] organic semiconductors,[12] fluorescent probes, and photoswitches.[9] Their strong intramolecular charge-transfer (ICT) behavior and ease of structural modification also make them promising candidates for applications in optoelectronics, including organic light-emitting diodes (OLEDs), photorefractive materials, and solar-energy-harvesting systems.[12–14] These versatile photophysical properties position chalcone-based materials as valuable building blocks for the development of advanced molecular photonic and electronic materials.

A diverse spectrum of metallic nanoparticles commands significant attention due to their remarkable potential across a range of applications. Among these, gold nanoshells (NSs) stand out as particularly noteworthy, owing to their unique structural and optical properties.[15] NSs consist of a dielectric core, typically composed of silica, surrounded by a thin gold shell. Their exceptional optical characteristics, such as tunable surface plasmon resonance, arise from the interplay between the core size and the gold shell thickness. This tunability enables their optical response to be precisely adjusted across the visible and near-infrared regions. Furthermore, their surface can be functionalized with a variety of ligands, such as silica,[16] peptides,[17] human serum albumin (HSA) and folic acid,[18] PEG-SH,[19] or organic dyes.[20] This functionalization enables targeted delivery and enhanced interaction with specific biomolecules, making them highly effective for photothermal and photodynamic applications.[21] These versatile characteristics position NSs as a valuable innovation in nanomedicine and nanotechnology.[22]

A novel approach, presented in this study involves the conjugation of chalcones to NSs, achieved through the use of appropriate functional groups. This strategy creates nanohybrids that synergistically combine the inherent bioactivity of chalcones with the distinctive optical and electronic properties of NSs. The interaction between chalcones and the gold surface induces structural and electronic modifications, which can significantly influence the properties and behavior of the hybrid material. Elucidating these interactions at the molecular level is essential for optimizing the design and functionality of chalcone-functionalized NSs. These advanced nanohybrids hold great potential for diverse applications, including targeted drug delivery, advanced diagnostics, and environmental remediation, offering enhanced performance and novel functionalities.

Among the multitude of spectroscopic techniques available, transient excited-state absorption emerges as one of the most appropriate methods for the precise characterization of processes in hybrid nanomaterials after photoexcitation. Pump–probe optical absorption spectroscopy has emerged as a powerful technique to study the ultrafast dynamics of materials, providing time-resolved information on electronic transitions, energy transfer, and vibrational dynamics.[23–25] Contrary to fluorescence kinetics measurements, it provides information also on the population of non-emissive states. In the context of chalcone-functionalized NSs, pump–probe experiments offer a unique opportunity to investigate the interplay between the chalcone molecules and the nanoparticle surface.

This manuscript explores the synthesis, characterization, and potential applications of novel chalcones and chalcones-functionalized gold NSs. To gain deeper insights into their excited-state dynamics and photophysical properties, transient optical absorption spectroscopy was employed. These measurements provided crucial information on excited-state lifetimes, energy transfer pathways, and the role of chalcone functionalization in modulating the electronic properties of NSs. The study highlights the chemical strategies for chalcone functionalization, the influence of chalcone attachment on the properties of NSs, and the emerging applications of these hybrid materials in therapeutics, diagnostics, and environmental remediation. By merging the chemistry of chalcones with the distinctive properties of NSs, these materials are positioned as a promising innovation in nanotechnology and materials science.

Experimental

Materials and methods

All the reagents and solvents were purchased from Merck Chemical Co. and POCh Gliwice and employed without further purification. Melting points (uncorrected) were determined on the Boëthius apparatus (type PHMK 05, Germany). Thin Layer Chromatography (TLC) was conducted on silica gel 60F254 aluminium sheets with QF-254 indicator eluting with chloroform/methanol 9/1 v/v mixture using UV light irradiation for visualization. Flash column chromatography was performed using silica gel 60 Å (220–440 mesh) eluting with dichloromethane/methanol 95/5 v/v mixture.

^{1}H and ^{13}C NMR spectra were recorded on a Bruker Ascend™ 400 NMR spectrometer using DMSO-d_6 as the solvent. Tetramethylsilane (TMS) served as the internal standard. The IR spectra were recorded in the range 400–4500 cm^{-1} on compounds embedded in KBr pellets using a Bruker ALPHA FT-IR spectrophotometer with the spectral resolution < 2 cm^{-1}.

All HRMS experiments were conducted using the LCMS-9030 qTOF system (Shimadzu, Kyoto, Japan), equipped with a standard SI source and the Nexera X2 system. Analyses were performed in positive ion mode across a mass-to-charge ratio (*m/z*) range of 50–2000. The LCMS-9030 parameters were as follows: nebulizing gas (nitrogen) flow rate of 3.0 L min^{-1}, drying gas flow rate of 10 L min^{-1}, heating gas flow rate of 10 L min^{-1}, interface temperature of 300 °C, desolvation line temperature of 400 °C, detector voltage of 2.02 kV, and interface voltage of 4.0 kV. The injection volume was adjusted within the range of 0.1 to 1 mL based on the signal intensity observed in the mass spectrum.

A Shimadzu UV-vis Multispec-1501 spectrophotometer and a Hitachi F-7100 spectrofluorimeter were used to record the absorption and emission spectra of the synthesized organic compounds, respectively. The samples were measured in quartz cells with a 1 cm optical path at room or liquid nitrogen temperature. The synthesized trimethoxysilylazachalcones were dissolved in solvents of varying polarity, including 1,4-dioxane (1,4-Dx), ethyl acetate (EtOAc), ethanol (EtOH), and *N*,*N*-dimethylformamide (DMF). The fluorescence quantum yield (ϕ_{FL}) of the compounds in EtOH was calculated by the comparative method using Rhodamine B (λ_{EX} = 450 nm) or Rhodamine 6G (λ_{EX} = 490 nm) in EtOH as a ref. 26.

Zeta potential measurements of the colloidal solutions of nanoparticles were performed on a Malvern Zetasizer Ultra Red. Nanoparticles were further charecterized with a FEI Tecnai G2 20 X-TWIN high-resolution transmission electron microscope (HRTEM) equipped with EDX. For imaging, ethanol-based nanoparticle solutions were deposited onto TEM grids, allowed to dry, and then visualized. The scanning electron microscopy (SEM) images were obtained using a Thermo Fisher SCIOS 2 system. Steady-state optical absorption spectra of the nanomaterial solutions were obtained using a Shimadzu UV-1900i spectrophotometer, with measurements taken in a 1 cm quartz cuvette.

The femtosecond pump probe laser system consisted of Mantis (Coherent, USA) seeded regenerative amplifier (Legend Elite, Coherent, USA) producing 2.1 W power at 1 kHz repetition rate centered around 800 nm. Pump wavelengths were generated from commercial optical parametric amplifier (TOPAS C, Light Conversion, Lithuania). We probed 430–830 nm region using a 3 mm sapphire crystal as a source of white light continuum. A magic angle (54.7°) polarization was always maintained to eliminate any rotational contributions. The instrument response function of our setup at this experimental configuration was around 160 fs. The solution phase measurements were performed in a continuously stirred 2 mm cuvette keeping the pump power around 1 μJ per pulse. The absorbance of the solution at the excitation wavelength was usually kept below 0.2.

The raw transient absorption data were background subtracted and chirp corrected with Surface Xplorer 4 (Ultrafast Systems, USA) and finally analysed by global analysis using Glotaran software package.

Computational part

Simulations were performed for the studied trimethoxysilylazachalcones, in cationic form, **4N1Si**, **4N2Si**, **3N1Si**, **3N2Si**, and their precursors **4N1**, **4N2**, **3N1**, **3N2** at the CAM-B3LYP/6-311++G(d,p) level of theory[27,28] in Gaussian program.[29] The solvent effects (EtOH) were taken into account by SMD-PCM model.[30] Geometries of studied compounds were optimized at the ground state with further evaluation of Hessians to confirm that the minima was found. Electronic structure properties and Ciofini's charge transfer parameters[31,32] were computed at the optimized ground state geometries.

Synthesis of trimethoxysilylazachalcones

Preparation of azachalcones based on an adopted procedure developed by Szücs *et al.*,[33] is described in our previous paper.[34] Trimethoxysilylazachalcones were synthesized by our method based on the general principles of alkylation of heterocyclic compounds and the methodology described by Iken *et al.*[35] The synthetic route used for their preparation is shown in Fig. 2.

Azachalcones with 3-trimethoxypropyl functionality enabling condensation with silica surface OH groups were synthesized by alkylation of the nitrogen in pyridine moiety with 3-iodopropyltrimethoxysilane (Fig. 2). Modification of the dyes structure with silane support was proved by ^{1}H and ^{13}C NMR measurements. In the ^{1}H NMR spectra of the trimethoxysilylazachalcones (see SI file) signals of the hydrogen atoms of the propane-1,3-diyl group around 4.6, 2.0 and 0.6 ppm and the methoxy group at *ca.* 3.5 ppm could be distinguished. The appearance of peaks of propane unit and methoxy groups proved the successful alkylation of the azachalkones with the 3-iodopropyltrimethoxysilane in all cases. Additionally, in the spectra of **4N1** and **3N1** the singlet of the 4-NMe$_2$ group appeared at *ca.* 3.1 ppm. The ^{13}C NMR spectra revealed corresponding peaks in the range of 185–112 ppm assigned to methine carbon (–CH=) and aryl carbons and in the range of 183–184 ppm to carbon in the carbonyl group (CO). The signal of the methoxy group at 50.6 ppm as well as those assigned to the carbon atoms of the propyl group (around 63–64 ppm, 25 ppm and 6 ppm) support the formation of a covalent bond between the azachalcone fragment and the silicate *via* the propylene spacer.[36] General method for the synthesis of trimethoxysilylazachalcones together with analysis of ^{1}H and ^{13}C NMR and IR spectra and all spectra are included in SI.

Nanoparticles synthesis

Gold nanoshells (NSs). All chemicals used in this study were obtained from Sigma-Aldrich, except for 120 nm silica nanoparticles, which were purchased from nanoComposix (U.S.). The synthesis of NSs was adopted from the protocol described by the Halas group[15,37] with some modifications[38] First, a 1% solution of tetrachloroauric(III) acid was prepared in deionized water and stored in the dark for at least 10 days prior to use.

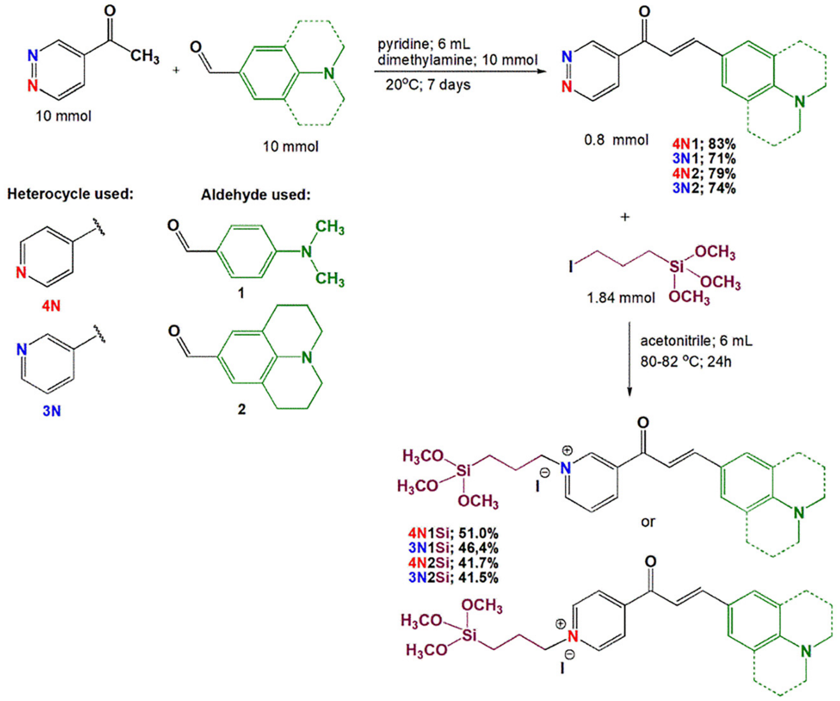

Fig. 2 General procedure for the synthesis of the trimethoxysilylazachalcones. Red and blue colors show the position of nitrogen in the heterocycle (pyridine ring), while green color represents two donor groups implemented in the studied structures (*N*,*N*-dimethylaniline and julolidine, respectively); the percent yields are given next to the abbreviations.

Then, a colloidal suspension of gold with tetrakis(hydroxymethyl)phosphonium chloride (THPC; 80% in H_2O), was prepared by mixing THPC, NaOH(aq) (1 M), and the aged 1% tetrachloroauric(III) acid solution. This suspension was stored in a refrigerator for at least 14 days before use. For the plating solution, 50 mg of potassium carbonate was dissolved in 200 mL of deionized water, followed by the addition of 3 mL of aged gold chloride solution. The mixture was stored in the dark for three days before use.

To coat the 120 nm silica nanospheres with (3-aminopropyl)triethoxysilane (APTES, 99.99%), 7 mL of silica nanosphere solution was diluted with deionized water to 42 mL, centrifuged twice at 3000 rcf for 25 minutes, and resuspended in 40 mL of ethanol. This solution was transferred to a plastic bottle, 400 μL of APTES was added, and the mixture was stirred overnight. After centrifugation and washing, the particles were resuspended in 20 mL of ethanol. For the preparation of gold seeds (1.5–3 nm) on APTES-coated silica nanospheres, 20 mL of colloidal THPC gold was placed in a glass container, to which 500 μL of 1 M sodium chloride solution and 4 mL of PC 120 were added. The mixture was stirred overnight, centrifuged twice at 1500 rcf for 20 minutes, and resuspended in 10 mL of water.

To synthesize NSs, 3 mL of the plating solution was placed in a plastic cuvette, and an appropriate volume of the seed solution was added. Next, 15 μL of formaldehyde was rapidly introduced, and the resulting mixture was vigorously shaken for 2 minutes. To scale up the synthesis, the plating solution, seed solution, and formaldehyde were combined in the desired proportions, stirred for 10 minutes, and centrifuged twice at 350 rcf for 20 minutes. The resulting suspension was resuspended in 10 mL of water and stored in a refrigerator.

Gold nanoshells with silica (NSs@SiO_2). The silica coating procedure was performed according to our previously described protocol.[16] In a glass vessel, 3 mL of scaled-up NSs solution was added to 4 mL of deionized water and mixed. Ethanol, ammonia water, and 2 μL of tetraethoxysilicate were added dropwise, and the solution was gently stirred overnight. The mixture was centrifuged twice for 20 minutes and resuspended in 10 mL of ethanol before being stored in the refrigerator.

Gold nanoshells with silica functionalized with trimethoxysilylazachalcones. Dye solutions with a concentration of 2 mg mL^{-1} in ethanol were prepared, sonication was required for dissolution. In a glass vial, 5 mL of NSs@SiO_2 solution was mixed with 1 mL of the prepared dye solution. The mixture was covered with aluminum foil and left stirring gently overnight. Subsequently, the mixture was centrifuged once for 20 minutes at 280 rcf. The supernatant was collected (centrifugation proceeded efficiently, allowing the complete recovery of the supernatant) and dispersed in 5 mL of ethanol.

Results and discussion

Spectroscopic properties of the trimethoxysilylazachalcones

Spectra of the synthesized compounds were measured in solvents of different polarity depending on the dielectric constant (ε_r): 1,4-dioxane (1,4-Dx, ε_r = 2.20), ethyl acetate (EtOAc,

ε_r = 6.02), ethanol (EtOH, ε_r = 24.55) and *N*,*N*-dimethylformamide (DMF, ε_r = 36.76). The electronic absorption spectra of the trimethoxysilylazachalcones and their precursor in EtOH are shown in Fig. 3.

The shape of the electronic absorption spectra of trimethoxysilylazachalcone is similar to that of chalcones, but the red shift of all bands occurs due to alkylation of the heterocyclic nitrogen atom (Fig. 3 and Fig. S1, SI). From the work of Harborne *et al.*[39] it follows that the two main observed absorption bands of azachalcone: long-wave (LW) and short-wave (SW) are related to its chemical structure, *i.e.* the band in the range of 390–500 nm is related to the B-ring cinnamoyl system, while the second relatively insignificant band with a maximum at about 280 nm comes from the A-ring (iso)nicotinoyl system (Fig. S1, SI). The long-wavelength band of azachalcone with a maximum in the visible region is responsible for their color.[4,40] Depending on the chemical structure and type of substituents in the molecule, a barely visible shoulder-shaped absorption peak appears at 340–350 nm, which is usually not detectable.[4]

In the case of trimethoxysilylazachalcones, the UV-visible spectra also show typical absorption bands for azachalcones with several maxima (Fig. 3B and Fig. S1, S2, SI). According to the literature data,[34,41,42] they result from the donor–acceptor structure of the molecule, where the long-wavelength band with maximum in the range from 464 to 559 nm comes from the $S_0 \rightarrow S_1$ transition generating an overlapping peak that originates from two absorption lines for all the compounds studied (Fig. S3, SI). This suggests the existence of a zwitterionic mesomer as a result of the n–π* transition in conjugated sequences involving –CO–CH═CH– group due to ICT from amine nitrogen to carbonyl oxygen. The shorter wavelength bands up to approx. 350 nm are attributed to the π–π* and n–π* transitions in pyridine and aromatic rings.

The stiffening of the amino group by the propane bridge connected to the phenyl ring shifts the main absorption band to the red, which suggests that julolidine has stronger electron-donating properties than the dimethylamino group.[34,43] This effect is more pronounced for silyl derivatives of azachalcones because the trimethoxysilyl group, which has electron-donating properties, makes the π electron system richer and consequently reduces the ionization potential. In the **4N2Si** compound, the rotation of the alkylamine group is not possible. It results in a planar structure and, hence, relatively low-energy transitions, causing the absorption maxima located at the longest wavelength. Contrary, the compound **3N2Si**, containing a 3-pyridyl moiety with weaker electron-withdrawing properties and an unstiffened *N*,*N*-dimethylamino electron-donating group, reveals the most significant blue shift because electron transfer is hindered by the twisting of the molecule. The influence of substituents on the absorbance and emission spectra of all compounds is shown in Fig. 3 as well as Fig. S2–S5.

The emission spectra of the studied compounds reveal significant shifts in the $\lambda_{\max}$ values depending on the electron-donating and electron-accepting properties of the individual structural units. The observed changes indicate a trend of decreasing fluorescence maxima from **4N2Si** to **3N1Si**. This observation highlights the influence of the secondary amine at the *para* position of the B ring of the molecule as well as the pyridinium moiety on the fluorescent properties of azachalcones. Compounds containing a stiffening amine group and pyridine ring substituted in *para* position have longer emission wavelengths and lower energy levels.

The basic photophysical properties such as the wavelength at the maximum of the long-wavelength absorption and fluorescence band, the Stokes shift, the molar extinction coefficient and fluorescence quantum yield in EtOH are listed in Table 1.

For the other solvents, the data are presented in Table S1, SI. The position of the absorption band as well as fluorescence of all synthesized compounds also depends on the solvent properties (see Table S1 and Fig. S1, S4, S6, SI). Compounds **4N1Si** and **4N2Si** show a change in absorption wavelength from 478 nm to 503 nm and from 526 nm to 559 nm, respectively, with varying

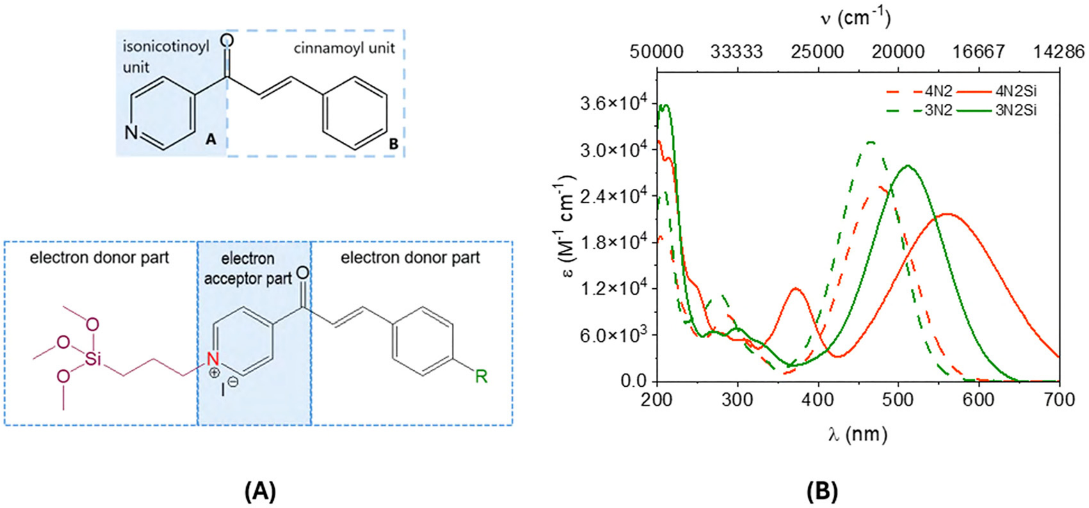

Fig. 3 (A) Structural moieties of trimethoxysilylazachalcone (as an example of responsible for the main bands in its absorption spectrum; (B) UV-Vis spectra of azachalcones and their trimethoxysilylated derivatives in EtOH.

Table 1 The basic spectroscopic parameters of the tested trimethoxysilylazachalcones, *i.e.*, absorption maxima of the long-wavelength band ($\lambda_{\max}^{\mathrm{Ab}}$), maximum extinction coefficient (ε), fluorescence maxima ($\lambda_{\max}^{\mathrm{Fl}}$), Stokes shift ($\Delta\nu^{\mathrm{SS}}$) and fluorescence quantum yield (ϕ_{Fl}) in EtOH

	4N1Si	4N2Si	3N1Si	3N2Si
$\lambda_{\max}^{\mathrm{Ab}}$ (nm)	503	559	469	511
ε (10^4 M^{-1} cm^{-1})	2.05	2.17	2.23	2.79
$\lambda_{\max}^{\mathrm{Fl}}$ (nm)	781	831	718	754
$\Delta\nu^{\mathrm{SS}}$ (cm^{-1})	7077	5855	7394	6307
ϕ_{Fl} (%)	0.024	0.022	0.063	0.029

solvent polarity. These values and the analysis of the spectra in Fig. S1 and S4 indicate a bathochromic shift of the long-wavelength n–π* band when changing the solvent from 1,4-dioxane to ethanol. Thus, these compounds exhibit positive solvatochromism, which means better stabilization of the excited state due to the stronger interaction of polar solvents with the molecules. This results in a decrease in the energy required for excitation and the energy difference between the ground and excited states, which causes a shift of the absorption spectrum to the red.[42,44] In the case of compounds **3N1Si** and **3N2Si** the position of the absorption band does not depend significantly on the polarity of the solvent. The lack of correlation is probably due to fairly similar polarities of the excited state and the ground state of these molecules, and thus the energy gap is barely influenced by the increasing polarity of the solvent.[45,46]

The fluorescence intensity, especially in polar solvents, is low due to fluorescence quenching. The fluorescence quantum yield of all the compounds in EtOH does not exceed 0.1% (Table 1), which indicates that the energy of the excited state is lost mainly by non-radiative processes. The shift of the emission band with respect to the absorption band in ethanol ranges from 5855 to 7394 cm^{-1}. This effect is illustrated for **3N1Si** in Fig. 4. As shown in Table S1, the Stokes shift increases with solvent polarity. Its values, with the exception of **4N1Si** in 1,4-dioxane, are high and exceed 1.4 × 10^3 cm^{-1}, indicating vibrational relaxation or loss of thermal energy prior to emission. Furthermore, the fluorescence and Stokes shift are influenced by the chemical structure related to the rigidity of the alkylamino group and the electron-withdrawing ability of the (iso)nicotinoyl unit (Table S1).

In general, increasing solvent polarity shifts fluorescence bands to the red. The broadening of the emission band in the polar environment indicates strong delocalization of π-electrons in the molecule which may suggest the generation of a CT state from any locally excited (LE) state.[4,41]

Theoretical calculations results

The experimental results were supplemented with theoretical calculations. We performed time-dependent density functional theory calculations at the CAM-B3LYP/6-311++G(d,p) level of theory.[27,28] The simulated one-photon excitation energies, Ciofini's charge transfer analyses, and the dominant molecular orbitals involved into the excitation for the precursors **3N1**, **3N2**, **4N1**, and **4N2**, and for the target compounds **3N1Si**, **3N2Si**, **4N1Si**, **4N2Si**, are presented in Tables S2 and S3, respectively.

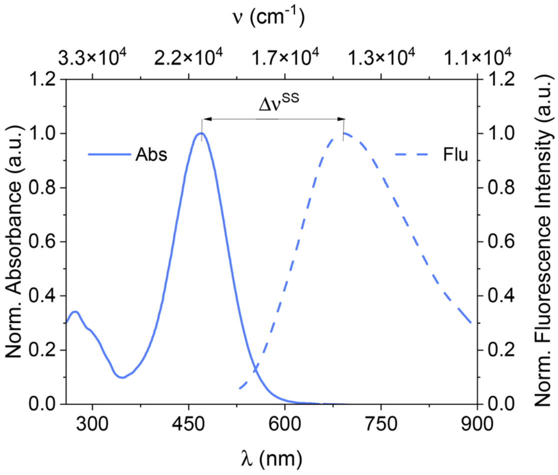

Fig. 4 UV-Vis and fluorescence spectra of **3N1Si** in EtOH illustrating the Stokes shift; excitation wavelength was 500 nm.

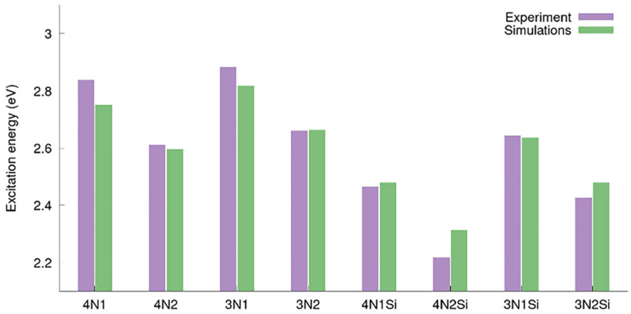

Fig. 5 Comparison of the energy of the experimental absorption maxima and simulated vertical excitation energies corresponding to $S_0 \rightarrow S_1$ transition, in ethanol solvent. Simulated vertical excitation energies were shifted by the same value (0.4 eV) to overlap with the experiment.

Computed excitation energies are in good agreement with experimental spectra, as demonstrated in Fig. 5; it confirms the reliability of the performed simulations.

Calculated excitation energies follow the observed experimental trends. Introduction of trimethoxysilyl group leads to red-shift of absorption spectra. Compounds with 4-pyridyl moiety, **4N1**, **4N2**, **4N1Si**, and **4N2Si**, have smaller excitation energies than compounds with 3-pyridyl group, **3N1**, **3N2**, **3N1Si** and **3N2Si**. Introduction of julolidine substituent, as in compounds **3N2**, **4N2**, **3N2Si** and **4N2Si**, leads to red-shift of absorption maxima in comparison to structures substituted with *N*,*N*-dimethylaniline, **3N1**, **4N1**, **3N1Si** and **4N2Si**.

The $S_0 \rightarrow S_1$ transition is the brightest, and for all compounds it is dominated by HOMO → LUMO one-electron transition (Tables S2 and S3, SI), therefore, the frontier molecular orbitals can approximately represent electronic density changes upon excitation. The frontier molecular orbitals (HOMO and LUMO) of precursors and target azachalcones are illustrated in Fig. S8–S15, SI. In Fig. 6 we present HOMO and LUMO of compound **4N2Si**, which confirms a well-pronounced charge-transfer character of the $S_0 \rightarrow S_1$ excitation.

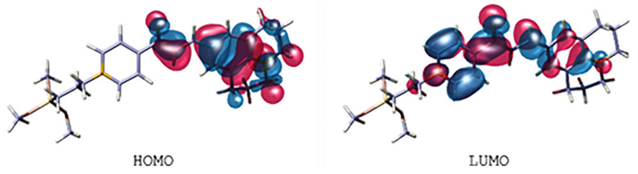

Fig. 6 Frontier molecular orbitals computed for compound **4N2Si**.

Table 2 Ciofini's charge transfer parameter D^{CT}

Without $(CH_3O)_3Si$	D^{CT} (Å)	With $(CH_3O)_3Si$	D^{CT} (Å)
4N1	3.76	**4N1Si**	4.18
4N2	3.75	**4N2Si**	4.18
3N1	3.68	**3N1Si**	3.82
3N2	3.68	**3N2Si**	3.82

In order to estimate the distance associated to a charge transfer of the excitation transitions, Ciofini's[27,28] charge transfer parameters D^{CT} were computed, the resulting values for $S_0 \rightarrow S_1$ excitation are shown in Table 2. All 4 target trimethoxysilylazachalcones exhibit significant intramolecular charge transfer upon the $S_0 \rightarrow S_1$ transition. They demonstrate greater parameters D^{CT} than the corresponding precursors without trimethoxysilyl group. Compounds with 4-pyridyl moiety have higher charge-transfer parameters D^{CT} than compounds with 3-pyridyl group. The highest charge transfer D^{CT} = 4.18 Å is observed for compounds **4N1Si** and **4N2Si**. Graphical representations of Ciofini's charge transfer parameters D^{CT} are given in Fig. S16–S23 for all investigated molecules, and in Fig. 7 we present visualization of D^{CT} for structure **4N2Si**. As can be seen, studied compounds undergo intramolecular charge transfer from cynnamoyl unit to acetylpyridine unit through the extended π-electron system.

Properties of NSs functionalized with silica-bound trimethoxysilylazachalcones

In the first stage of hybrid nanoparticle synthesis, we focused on fabricating NSs with a gold layer thickness of 21.6 ± 4.3 nm. Subsequently, a silica layer with a thickness of 5.2 ± 2.9 nm was added to avoid direct attachment of fluorescent emitters to the gold surface, which could lead to fluorescence quenching.[47] In the next step, an organic layer composed of trimethoxysilylazachalcones was created, the layer thickness ranges between 12.9 ± 4.0 nm and 27.2 ± 7.5 nm (Table 3). TEM images presented in Fig. 8 illustrate the prepared hybrid nanomaterials. The images demonstrate that the synthesized hybrid material exhibits a propensity to assemble into elongated structures, specifically chains composed of individual nanoparticles. A comparable phenomenon has been observed in our earlier studies involving gold nanorods coated with polymeric materials.[48] In both cases, the formation of such structures is likely governed by hydrogen bonding or electrostatic interactions

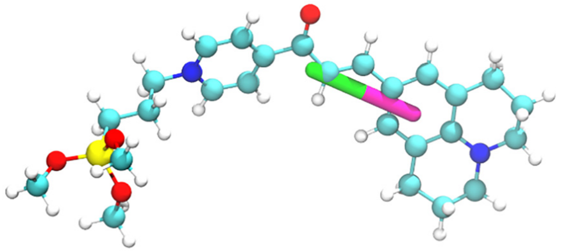

Fig. 7 Graphical representation of Ciofini's charge transfer parameter D^{CT} for compound **4N2Si**. Magenta colour represents depletion of the charge density, green colour represents increase of the charge density.

Table 3 Zeta potential values of the colloidal nanomaterials in ethanol, along with the thickness of the layer attached to the metallic surface

Sample name	Zeta pot. (mV)	Thickness of SiO_2 layer (nm)	Thickness of the organic layer on the SiO_2 layer (nm)
NSs	−41.66		
NSs@SiO_2	−47.76	5.2 ± 2.9	
NSs@SiO_2@**4N1Si**	52.65	5.2 ± 2.9	13.0 ± 3.2
NSs@SiO_2@**4N2Si**	36.93	5.2 ± 2.9	27.2 ± 7.5
NSs@SiO_2@**3N1Si**	46.54	5.2 ± 2.9	2.5 ± 3.3
NSs@SiO_2@**3N2Si**	42.94	5.2 ± 2.9	12.9 ± 4.0

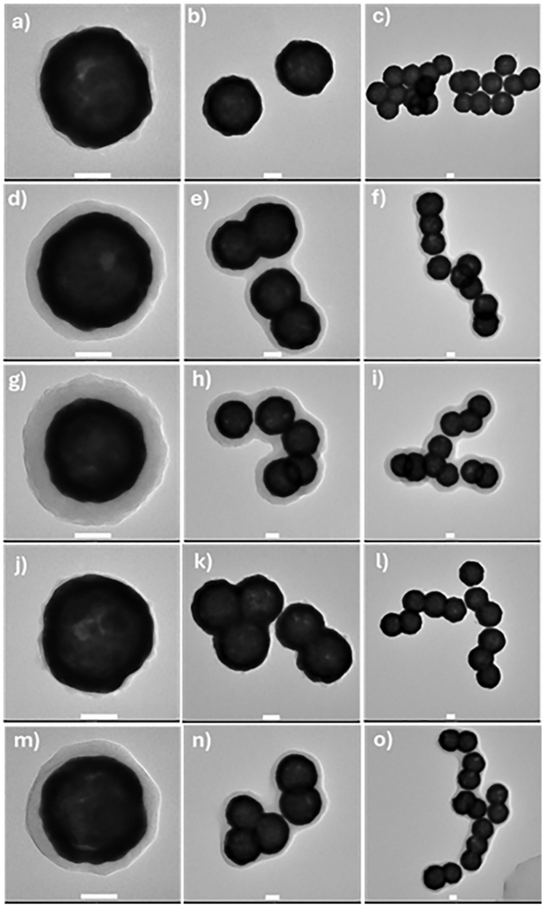

Fig. 8 Representative TEM images of NSs coated with a gold layer of thickness 21.6 ± 4.3 nm, and an additional silica layer of thickness 5.2 ± 2.9 nm (NS_S@SiO_2 a, b, c), subsequently coated with **4N1Si** (d, e, f), **4N2Si** (g, h, i), **3N1Si** (j, k, l), and **3N2Si** (m, n, o). The white line indicates a scale of 50 nm for each image.

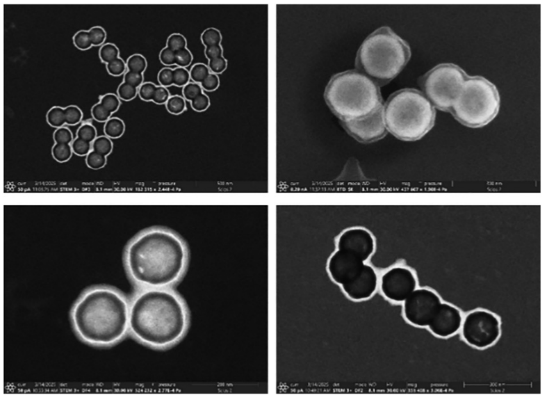

Fig. 9 SEM images of sample NSs@SiO_2 with **4N1Si**.

between the zwitterionic mesomeric forms of the chalcone molecule, involving the carbonyl group, which has a significant impact on the self-assembly, see the illustration of the mechanism in Fig. S24, SI. To provide a clearer visualization of the nanostructures and to reveal the surface morphology of the nanoparticles, we additionally performed SEM measurements. The results are presented in Fig. 9.

The changes occurring on the surface of NSs during the hybrid material formation stage significantly influence the recorded extinction spectrum of the solution (see Fig. S25, SI). A notable broadening of the extinction band of the NSs was observed, along with its shift toward longer wavelengths. This phenomenon was also encountered during the formation of dimers and trimers, between NSs, indicating the possibility of surface plasmon propagation between nanoparticles.[16,48] The extinction spectra of the hybrid nanomaterial solution reveal well-defined absorption bands assigned to trimethoxysilylazachalcones in both the LW and SW regions. The EDX spectra presented in Fig. S26 further confirm the presence of trimethoxysilylazachalcones on the surface of the NSs.

The absolute zeta potential values for all investigated systems, see Table 3, including NSs, silica-coated NSs, and silica-coated NSs functionalized with trimethoxysilylazachalcones, exceed 30 mV. This threshold is a critical indicator of colloidal stability, as it signifies strong electrostatic repulsion between particles.[49] In colloidal systems, a zeta potential with an absolute value greater than 30 mV, whether positive or negative, is generally associated with stable dispersions, as the electrostatic forces prevent particle aggregation. For NSs and silica-coated NSs with negative zeta potentials, the stability arises from repulsion due to the similarly charged surfaces. A negative zeta potential of NSs in water can be attributed to the ionization of hydroxyl groups or adsorbed ions on their surface, which creates a negatively charged interface. NSs coated with silica retain a negative zeta potential in ethanol due to the deprotonation of silanol groups on the silica layer, which imparts a net negative charge to the surface. Similarly, silica-coated NSs functionalized with trimethoxysilylazachalcones in ethanol exhibit a strong positive zeta potential exceeding 30 mV. This ensures sufficient repulsive interactions to maintain colloidal stability, even after charge inversion due to surface functionalization. The overall positive potential arises from protonated amino or other cationic groups, such as pyridinium, within the azachalcone molecules, which dominate the surface charge.

Another important aspect to highlight is the change in the emission bands of the trimethoxysilylazachalcone upon attachment to the NSs (compare Fig. S6 and S27, SI). In all cases, the emission maximum was red-shifted by approximately 30 nm. Furthermore, for the hybrid nanomaterials with compounds **4N1Si** and **4N2Si**, a significant broadening of the emission band was observed, along with the emergence of an additional band at shorter wavelengths. Previous studies[34] have shown that the emission originates from two mesomeric forms of azachalcone derivatives. Upon binding to NSs, this dual emission becomes even more pronounced, as evidenced by the clear appearance of two separate emission bands. Notably, in case of the *para*-conFig.d azachalcones, the emission from the two zwitterionic mesomeric forms becomes more distinct upon attachment to the NSs, which may result from stronger electrostatic interactions and the formation of hydrogen bonds in the hybrid nanostructures. It suggests that during the formation of the trimethoxysilylazachalcone layer on the surface of the NSs, the *Z* (*cis*) isomer is stabilized.

Transient absorption spectroscopy of trimethoxysilylazachalcone

Fig. 10 shows the most representative results of the spectral evolution profiles for all four trimethoxysilylazachalcone samples dissolved in ethanol. The **4N1Si**, **4N2Si**, **3N2Si** samples were excited at a wavelength of 570 nm, the sample **3N1Si**, was excited at 500 nm due to a blue-shifted absorption band. The spectral evolution plots reveal distinct spectral features: (i) excited-state absorption (ESA) observed in the range of approximately 430–470 nm; (ii) ground-state bleach (GSB) occurring between approximately 470 nm and 600 nm, depending on the steady state absorption; and (iii), additional excited-state processes at longer wavelengths, which can be attributed to intramolecular charge transfer.[50] In 4N-series (**4N1Si** and **4N2Si**), distinct ESA features are observed immediately after excitation (~500 fs) in the 440–475 nm and 650–750 nm regions, along with a GSB resembling the steady-state absorption, marked as dote lines in the graphs. The ESA at longer wavelengths shows a gradual blue shift as the delay increases, with all features decaying within ~50 ps. In the 3N-series (**3N1Si**, **3N2Si**), the ESA overlaps with the 650–750 nm region, where stimulated emission (SE) also contributes. Compared to the 4N-series, the ESA displays a stronger blue shift, while the GSB and SE features evolve simultaneously. In this case, all excited-state signals decay within ~100 ps.

Using a sequential three-state kinetic model with the Glotaran program package,[51] the global analysis of the 4N and 3N series (Fig. S28) revealed a rapid decay of the excited-state signals, with lifetimes predominantly in the sub-picosecond to few-picosecond range. This behavior is consistent with efficient intramolecular charge transfer[52,53] (ICT, Table S2 and S3), followed by ultrafast non-radiative relaxation. The fast

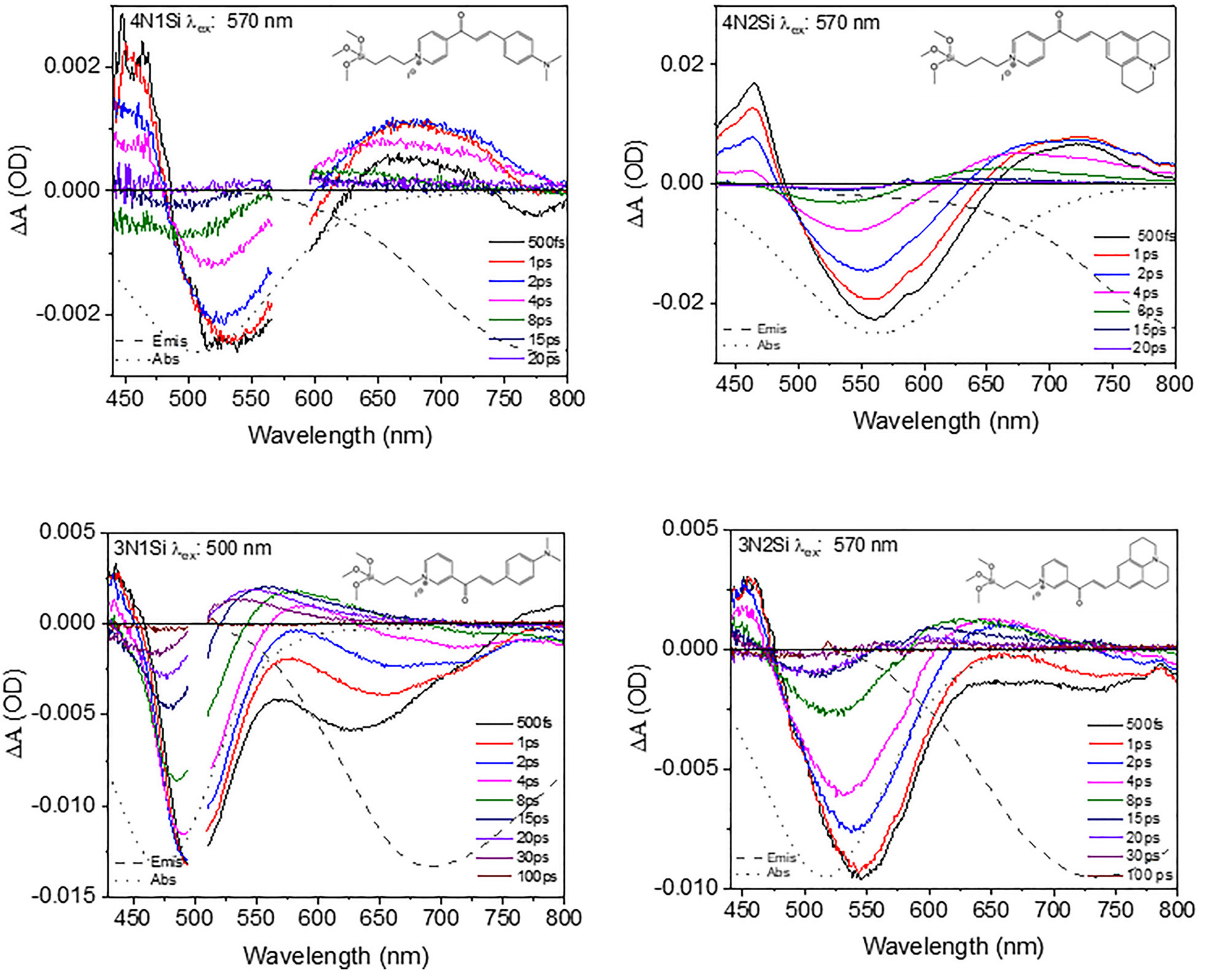

Fig. 10 Spectral evolution of trimethoxysilylazachalcones: **4N1Si**, **4N2Si**, **3N1Si**, **3N2Si** in ethanol solution. The excitation wavelengths are indicated in the panels. The dotted line represents the inverted absorption spectrum, while the dashed-dotted line depicts the inverted emission spectrum.

dynamics align with the strong donor–acceptor coupling and extended conjugation present in the 4-position-bridged systems, which facilitate rapid charge separation and recombination.

In contrast, the 3N series exhibits a rapidly evolving SE band in the initial stages of the dynamics (dashed lines in Fig. 10), alongside GSB and ESA. The SE persists over the few-picosecond timescale, observed particularly in **3N2Si**, indicating the formation of a relatively long-lived excited state with significant locally excited (LE) character. The slower decay kinetics in the 3N series can be attributed to the meta (3-) position bridging, which reduces the efficiency of the ICT formation and stabilizes the LE state, thereby enhancing radiative decay pathways. Global lifetime analysis supports these assignments: while the 4N series exhibits very fast excited-state decay (all components <7 ps), the 3N series shows substantially longer-lived states (up to 12.6 ps). These results are in line with the observed SE, the blue-shifted steady-state absorption, and previously reported sub-picosecond ICT dynamics in dimethylamino-chalcones and related push–pull systems.[52,54] To better rationalize the lifetimes summarized in Table 4, we consider the influence of the substituent in the *para* position. The shortest lifetime components can be assigned to vibrational cooling and internal conversion from higher vibrational levels of the S_1 state or from upper electronic states to the lower regions of the S_1 potential energy surface. For **4N2Si**, this component is slightly longer (0.7 ps), consistent with the structural rigidity imposed by the julolidine core, which introduces a modest barrier to vibrational relaxation and initial structural reorganization from the Franck–Condon region. In contrast, the more flexible donor in **4N1Si** enables a slightly

Table 4 Lifetimes of the three processes associated with the excited state relaxation for samples: **4N1Si**, **4N2Si**, **3N1Si**, **3N2Si** in ethanol together with their quantum yields

Compound	τ_1 (ps)	τ_2 (ps)	τ_3 (ps)	FL QY (%)
4N1Si	0.5	3.4	6.2	0.024
4N2Si	0.7	1.9	5.6	0.022
3N1Si	0.8	6.5	7.1	0.063
3N2Si	1.4	11.5	12.6	0.029

faster decay (0.5 ps), as fewer conformational adjustments are required to reach the relaxed excited state. After overcoming the initial reorganization barrier, the ICT state in **4N2Si** stabilizes more rapidly (1.9 ps), reflecting enforced planarity and efficient donor–acceptor orbital overlap. Conversely, the flexible donor in **4N1Si** requires more time (3.4 ps) to reach equilibrium through solvation and conformational adjustment, indicating a broader distribution of intermediate states. In the final decay stage, the rigid structure in **4N2Si** promotes slightly faster relaxation from the ICT state back to the ground state (5.6 ps), consistent with strong vibronic coupling and efficient deactivation pathways. The slower decay observed in **4N1Si** (6.4 ps) suggests a less well-defined ICT state that couples less effectively to non-radiative deactivation channels. The observed fluorescence quantum yields (Table 4) correlate well with this dynamics: molecules exhibiting more efficient non-radiative decay (4N series) display both lower quantum yields and shorter lifetimes, whereas those with slower non-radiative decay (3N series) show higher quantum yields and longer lifetimes. This is consistent with the presence of SE and the persistence of excited-state populations in the time-resolved data.[55–57]

Transient absorption spectroscopy of hybrid nanomaterials

To gain insight into the interactions between the plasmonic NSs and the trimethoxysilylazachalcone layer, we performed transient absorption measurements on the colloidal solutions of NSs@SiO_2 and hybrid nanomaterial. Here, we focus on the results obtained for the NSs@SiO_2@**4N2Si** sample – hybrid nanomaterial, as it exhibited the most distinctive features, see Fig. 11 and Fig. S29, SI.

Before we go into interpretation of the excited-state dynamics of the hybrid material-NSs@SiO_2@**4N2Si**, we first measured the reference system of **4N2Si** (already described in previous section) and bare NSs@SiO_2 dispersed in ethanol. According to the literature, transient absorption spectroscopy of plasmonic nanoparticles reveals lifetimes of electron–phonon recombination and phonon–phonon scattering on the picosecond timescale. Heating of the nanoparticle lattice and lattice phonon interactions are reflected in the visible and NIR regions as oscillations of bleaching peaks, corresponding to the extensional and breathing modes of coherent acoustic phonon vibrations.[58,59] In our studies NSs@SiO_2 exhibit a broad GSB signal corresponding to the bleaching of their LSPR, which spans from approximately 600 nm to 775 nm with a maximum at 688 nm. Concurrently, a distinct ESA band is present around 516 nm, likely cause by interband transitions of hot electrons. Both the LSPR bleach and the ESA features of isolated NSs display long-lived decay dynamics, persisting well beyond 30 ps and, as noted, extending into the nanosecond regime. This behavior is characteristic of the slow thermal relaxation of hot carriers generated following non-radiative plasmon decay. In the following step, we investigated the hybrid material – NSs@SiO_2@**4N2Si**. To facilitate interpretation, we compared its behavior with that of NSs@SiO_2 and compound **4N2Si**, and prepared an overlaid spectrum for direct comparison, see Fig. 11. The pronounced extension of excited-state lifetimes observed upon covalent anchoring of trimethoxysilylazachalcones to NSs is a significant finding. Long-lived ICT states of this magnitude are uncommon in organic-plasmonic hybrid systems, highlighting the strong influence of plasmon–molecule interactions on excited-state dynamics. This enhancement reflects the combined effects. Importantly, such prolonged lifetimes are directly relevant for applications requiring sustained excited states, including optical sensing, stabilization of charge-separated states, and photonic or biomedical technologies. By establishing this context, we provide a framework for the subsequent discussion of the potencial mechanistic origins of the observed phenomena. In NSs@SiO_2@**4N2Si** transient spectrum is composed of an ESA near 500 nm (closer to NSs@SiO_2 band than to free **4N2Si**) and a broad, partially suppressed GSB spanning from around ≈620 to 800 nm with reduced amplitude near ∼730 nm. The long-lived character of the hybrid's signals (persisting to 6 ns) closely follows the NSs@SiO_2 dynamics rather than the rapid molecular decay observed for free **4N2Si** (see Fig. S29, SI). Representative time profiles of normalized TA recorded at 450 nm illustrate the differences in characteristic timescales between the systems (see Fig. S29, SI). This behavior indicates that NSs@SiO_2@**4N2Si** substantially can modify the molecular excited-state dynamics; plausible contributions include plasmon-mediated modification of molecular excited states, stabilization of long-lived interfacial states, and spectral overlap of the NSs@SiO_2 response onto the molecular bands. We therefore interpret the hybrid TA as a superposition of the intrinsic, long-lived NSs@SiO_2 response and a perturbed molecular response whose spectral position and lifetime are altered by strong electronic and thermal coupling to the metal. Under femtosecond laser irradiation, excitation of the LSPR in the gold core generates a strongly enhanced electromagnetic field in the immediate vicinity of the nanoparticle.[60] This local field perturbation can modify the electronic structure of the attached organic molecules, reducing non-radiative decay and thereby stabilizing their excited states. Moreover, ultrafast hot electron generation and subsequent transfer from the nanoparticle to the molecule's LUMO can lead to the formation of

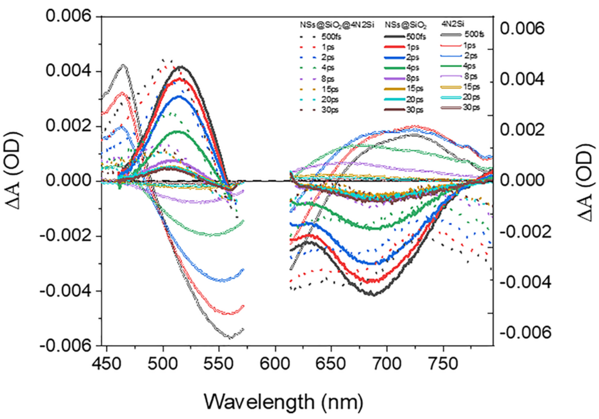

Fig. 11 Comparison of spectral evolution for: NSs@SiO_2, **4N2Si** and NSs@SiO_2@**4N2Si** in ethanol solution, excited at 570 nm.

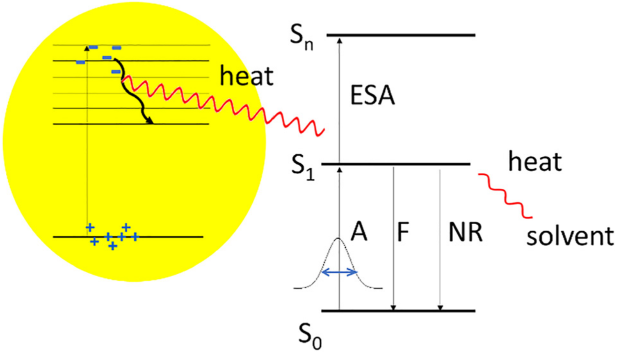

Fig. 12 Diagram illustrating the changes within the hybrid system following femtosecond-pulse absorption, followed by heat dissipation to the surroundings on the nanosecond timescale. F – fluorescence; A – absorption; NR – non-radiative processes.

charge-separated states with significantly longer lifetimes. The establishment of such states is further supported by strong electronic coupling at the metal-molecule interface, which facilitates efficient charge injection while suppressing rapid recombination. Additionally, molecular attachment to the nanoparticle surface restricts conformational flexibility and passivates non-radiative decay channels, further contributing to the suppression of internal conversion processes. Although all these processes are in principle possible, it is important to note that nanoparticle heating and subsequent heat release can occur on the nanosecond timescale.[61] As a result, a significant fraction of the weaker molecular contributions becomes difficult to isolate, as they are effectively masked by the dominant thermal response. Below, a schematic overview of the photophysical processes occurring in the hybrid material is presented (Fig. 12). Although multiple pathways may contribute, the primary mechanism responsible for the prolonged TA signal is the heat generation associated with the NSs.

Conclusions

A new method has been developed for the synthesis of trimethoxysilylazachalcones with pyridine A ring, compounds with a distinct donor–acceptor molecular architecture and therefore with strong intramolecular charge transfer (ICT), due to which they exhibit intriguing optical properties. Experimental studies as well as theoretical calculations have confirmed that chalcones with isonicotine unit (*p*-pyridine A ring, samples 4N) exhibit higher charge transfer efficiency than chalcones with nicotine unit (*m*-pyridine A ring, samples 3N). Further it was shown that the ICT is significantly enhanced by: (i) *N*-alkylation of pyridine A ring resulting in its ionization and thus a higher affinity to accept electrons, and (ii) introduction of a rigid julolidine group instead of a dimethylamino group in the electron-donating part of chalcone molecules. *N*-alkylation of pyridine A ring with 3-(trimethoxysilyl)prop-1-yl group enabled anchoring of chalcones to surfaces of plasmonic NSs giving hybrid materials with modulated excited state lifetimes, a unique optical behavior and promising biomedical relevance.

Femtosecond pump–probe spectroscopy revealed the excited-state dynamics in free dissolved molecules of ionic chalcones (**4N1Si**, **4N2Si**, **3N1Si**, **3N2Si**) and their gold-based hybrid systems (NSs@SiO_2@**4N2Si**). Attaching the chalcone to plasmonic gold nanostructures resulted to a remarkable increase in the excited state lifetime by three orders of magnitude, from 5.6 ps to 15 ns. It is therefore clear that plasmon–chalcone interactions significantly affect the transient absorption response of attached chalcone molecules. They induce significant changes in spectral characteristics, including absorption peak shifts, lifetime changes, and the formation of new transition states. This occurs mainly through mechanisms such as hot electron transfer, plasmon-exciton coupling, local field enhancement and dominant thermal effects.

The above findings highlight the potential of nanoscale plasmonic coupling as a strategy for engineering excited state dynamics to design tunable hybrid systems with substantially extended lifetimes. Such systems offer exciting opportunities for next-generation applications in light harvesting, targeted phototherapies, and time-resolved bioimaging, where precise control over ultrafast photoinduced processes is crucial.

Conflicts of interest

There are no conflicts to declare.

Data availability

The data is not publicly available apart from the data contained in the article or the supplementary information (SI). Supplementary information: ^1H and ^{13}C NMR spectra, MS spectra, electronic absorption and fluorescence spectra in solvents of different polarity (Fig. S1–S7), spectroscopic data (Table S1), computed electronic structure properties (Tables S2 and S3), frontier molecular orbitals (Fig. S8–S15), graphical representation of Ciofini's charge transfer parameter D^{CT} (Fig. S16–S23), proposed interaction mechanisms in hybrid nanomaterials formation (Fig. S24), normalized extinction spectra (Fig. S25), representative EDX spectra (Fig. S26), fluorescence spectra of NSs with silica and trimethoxysilylazachalcones (Fig. S27), evolution-associated difference spectra (Fig. S28), and temporal absorption profiles from exponential model fits and time course of normalized transient absorbance recorded at 450 nm (Fig. S29). See DOI: https://doi.org/10.1039/d5tc03618f.

Acknowledgements

This work was supported by the project No. UMO-2021/43/D/ST5/02249, SONATA 17, funded by National Science Center Poland (NCN). The authors thank Dr Remigiusz Bąchor for HRMS measurement. M. G.-W. acknowledges the support of the University of Wrocław under the program ''Initiative of Excellence Research University'' for funding the academic visit to a leading international institution (Agreement No. IDUB.29/2024). Authors acknowledge Mr Michał Pietrzak for his assistance in the synthesis of hybrid nanomaterials. Computational resources generously provided by the Wroclaw Center for Networking and Supercomputing are acknowledged.

Notes and references

1 H. A. Jasim, L. Nahar, M. A. Jasim, S. A. Moore, K. J. Ritchie and S. D. Sarker, *Biomolecules*, 2021, **11**, 1203.

2 C. Zhuang, W. Zhang, C. Sheng, W. Zhang, C. Xing and Z. Miao, *Chem. Rev.*, 2017, **117**, 7762–7810.

3 N. K. Sahu, S. S. Balbhadra, J. Choudhary and D. V. Kohli, *Curr. Med. Chem.*, 2012, **19**, 209–225.

4 A. Rammohan, J. S. Reddy, G. Sravya, C. N. Rao and G. V. Zyryanov, *Environ. Chem. Lett.*, 2020, **18**, 433–458.

5 P. Singh, A. Anand and V. Kumar, *Eur. J. Med. Chem.*, 2014, **85**, 758–777.

6 S. Verma, A. K. Srivastava and O. P. Pandey, *PharmaTutor*, 2018, **6**, 22–39.

7 D. I. Batovska and I. T. Todorova, *Curr. Clin. Pharmacol.*, 2010, **5**, 1–29.

8 P. Thapa, S. P. Upadhyay, W. Z. Suo, V. Singh, P. Gurung, E. S. Lee, R. Sharma and M. Sharma, *Bioorg. Chem.*, 2021, **108**, 104681.

9 L. Siddiqui, M. B. Hawsawi, G. A. Chotana and R. S. Z. Saleem, *ACS Omega*, 2024, **9**, 42061–42090.

10 M. Xu, P. Wu, F. Shen, J. Ji and K. P. Rakesh, *Bioorg. Chem.*, 2019, **91**, 103133.

11 J. M. F. Custodio, G. D. C. D'Oliveira, F. Gotardo, L. H. Z. Cocca, L. de Boni, C. N. Perez, H. B. Napolitano, F. A. P. Osorio and C. Valverde, *Phys. Chem. Chem. Phys.*, 2021, **23**, 6128–6140.

12 S. Kagatikar, D. Sunil, D. Kekuda, M. N. Satyanarayana, S. D. Kulkarni, Y. N. Sudhakar, A. K. Vatti and A. Sadhanala, *Mater. Chem. Phys.*, 2023, **293**, 126839.

13 V. S. Sharma, A. S. Sharma, N. K. Agarwal, P. A. Shah and P. S. Shrivastav, *Mol. Syst. Des. Eng.*, 2020, **5**, 1691–1705.

14 S.-J. Sun, G. Schwarz, H. R. Kricheldorf and T.-C. Chang, *J. Polym. Sci., Part A:Polym. Chem.*, 1999, **37**, 1125–1133.

15 B. E. Brinson, J. B. Lassiter, C. S. Levin, R. Bardhan, N. Mirin and N. J. Halas, *Langmuir*, 2008, **24**, 14166–14171.

16 M. Gordel-Wójcik, M. Pietrzak, R. Kołkowski and E. Zych, *J. Lumin.*, 2024, **270**, 120565.

17 S.-Y. Liu, Z.-S. Liang, F. Gao, S.-F. Luo and G.-Q. Lu, *J. Mater. Sci.: Mater. Med.*, 2010, **21**, 665–674.

18 A. Topete, M. Alatorre-Meda, P. Iglesias, E. M. Villar-Alvarez, S. Barbosa, J. A. Costoya, P. Taboada and V. Mosquera, *ACS Nano*, 2014, **8**, 2725–2738.

19 M. Gordel-Wójcik, K. Piela and R. Kołkowski, *Phys. Chem. Chem. Phys.*, 2022, **24**, 5700–5709.

20 Q. You, Q. Sun, M. Yu, J. Wang, S. Wang, L. Liu, Y. Cheng, Y. Wang, Y. Song, F. Tan and N. Li, *ACS Appl. Mater. Interfaces*, 2017, **9**, 40017–40030.

21 X. Huang, P. K. Jain, I. H. El-Sayed and M. A. El-Sayed, *Lasers Med. Sci.*, 2008, **23**, 217–228.

22 C. Loo, A. Lowery, N. Halas, J. West and R. Drezek, *Nano Lett.*, 2005, **5**, 709–711.

23 M. Mukherjee, S. Bhagat, M. A. Thottappali, P. Garg, A. I. Nurani, B. Satpati, S. Hussain, S. Pal, U. Deshpande, S. Sutradhar, J. Pfleger and G. Pramanik, *J. Phys. Chem. C*, 2024, **128**, 12259–12266.

24 Y. R. Panthi, M. A. Thottappali, P. Horáková, L. Kubáč, J. Pfleger, M. Menšík and T. Khan, *Chem. Phys. Chem.*, 2024, **25**, e202300872.

25 G. Pramanik, K. Kvakova, M. A. Thottappali, D. Rais, J. Pfleger, M. Greben, A. El-Zoka, S. Bals, M. Dracinsky, J. Valenta and P. Cigler, *Nanoscale*, 2021, **13**, 10462–10467.

26 A. M. Brouwer, *Pure Appl. Chem.*, 2011, **83**, 2213–2228.

27 R. Ditchfield, W. J. Hehre and J. A. Pople, *J. Chem. Phys.*, 1971, **54**, 724–728.

28 T. Yanai, D. P. Tew and N. C. Handy, *Chem. Phys. Lett.*, 2004, **393**, 51–57.

29 M. J. Frisch, G. W. Trucks, H. B. Schlegel, G. E. Scuseria, M. A. Robb, J. R. Cheeseman, G. Scalmani, V. Barone, G. A. Petersson, H. Nakatsuji, X. Li, M. Caricato, A. V. Marenich, J. Bloino, B. G. Janesko, R. Gomperts, B. Mennucci, H. P. Hratchian, J. V. Ortiz, A. F. Izmaylov, J. L. Sonnenberg, D. Williams-Young, F. Ding, F. Lipparini, F. Egidi, J. Goings, B. Peng, A. Petrone, T. Henderson, D. Ranasinghe, V. G. Zakrzewski, J. Gao, N. Rega, G. Zheng, W. Liang, M. Hada, M. Ehara, K. Toyota, R. Fukuda, J. Hasegawa, M. Ishida, T. Nakajima, Y. Honda, O. Kitao, H. Nakai, T. Vreven, K. Throssell, J. A. Montgomery, J. E. Peralta, F. Ogliaro, M. J. Bearpark, J. J. Heyd, E. N. Brothers, K. N. Kudin, V. N. Staroverov, T. A. Keith, R. Kobayashi, J. Normand, K. Raghavachari, A. P. Rendell, J. C. Burant, S. S. Iyengar, J. Tomasi, M. Cossi, J. M. Millam, M. Klene, C. Adamo, R. Cammi, J. W. Ochterski, R. L. Martin, K. Morokuma, O. Farkas, J. B. Foresman and D. J. Fox, *Gaussian 16, Revision C.01*, Gaussian, Inc., Wallingford CT, 2016.

30 A. V. Marenich, C. J. Cramer and D. G. Truhlar, *J. Phys. Chem. B*, 2009, **113**, 6378–6396.

31 T. Le Bahers, C. Adamo and I. Ciofini, *J. Chem. Theory Comput.*, 2011, **7**, 2498–2506.

32 C. Adamo, T. Le Bahers, M. Savarese, L. Wilbraham, G. García, R. Fukuda, M. Ehara, N. Rega and I. Ciofini, *Coord. Chem. Rev.*, 2015, **304–305**, 166–178.

33 L. Szücs, J. Ďurinda, L. Krasnec and J. Heger, *Chemické Zvesti*, 1966, **20**, 817–825.

34 M. Pietrzak, M. Józefowicz, A. Bajorek and J. R. Heldt, *J. Fluoresc.*, 2017, **27**, 537–549.

35 H. Iken, F. Guillen, H. Chaumat, M.-R. Mazières, J.-C. Plaquevent and T. Tzedakis, *Tetrahedron Lett.*, 2012, **53**, 3474–3477.

36 B. Adamcsik, E. Nagy, B. Urbán, P. Szabó, P. Pekker and R. Skoda-Földes, *RSC Adv.*, 2020, **10**, 23988–23998.

37 R. Bardhan, N. K. Grady and N. J. Halas, *Small*, 2008, **4**, 1716–1722.

38 M. Gordel, J. Olesiak-Banska, R. Kolkowski, K. Matczyszyn, M. Buckle and M. Samoc, *J. Mater. Chem. C*, 2014, **2**, 7239–7246.

39 J. B. Harborne, T. J. Mabry and H. Mabry, *The Flavonoids*, Springer, New York, 1st edn, 1975.

40 V. de Freitas and N. Mateus, *Environ. Chem. Lett.*, 2006, **4**, 175–183.

41 A. H. Romero, I. E. Romero, O. E. Piro, G. A. Echeverría, L. A. Gotopo, M. N. Moller, G. A. Rodríguez, G. J. Cabrera, E. R. Castro, S. E. López and H. E. Cerecetto, *J. Phys. Chem. B*, 2021, **125**, 9268–9285.

42 I. Chandrasekaran and S. Sarveswari, *RSC Adv.*, 2024, **14**, 30385–30395.

43 R. Gawinecki, E. Kolehmainen and R. Kauppinen, *J. Chem. Soc., Perkin Trans. 2*, 1998, 25–30, DOI: 10.1039/A705668K.

44 M. Homocianu, *Microchem. J.*, 2024, **198**, 110166.

45 M. Kong, T. Wang, X. Tian, F. Wang, Y. Liu, Q. Zhang, H. Wang, H. Zhou, J. Wu and Y. Tian, *J. Mater. Chem. C*, 2015, **3**, 5580–5588.

46 B. Jędrzejewska, B. Ośmiałowski and R. Zaleśny, *Photochem. Photobiol. Sci.*, 2016, **15**, 117–128.

47 E. Dulkeith, M. Ringler, T. A. Klar, J. Feldmann, A. Muñoz Javier and W. J. Parak, *Nano Lett.*, 2005, **5**, 585–589.

48 M. Gordel, K. Piela, R. Kołkowski, T. Koźlecki, M. Buckle and M. Samoć, *J. Nanopart. Res.*, 2015, **17**, 477.

49 J. D. Clogston and A. K. Patri, in *Characterization of Nanoparticles Intended for Drug Delivery*, ed. S. E. McNeil, Humana Press, Totowa, NJ, 2011, pp. 63–70, DOI: 10.1007/978-1-60327-198-1_6.

50 R. Ghosh and D. K. Palit, *J. Phys. Chem. A*, 2015, **119**, 11128–11137.

51 J. J. Snellenburg, S. Laptenok, R. Seger, K. M. Mullen and I. H. M. van Stokkum, *J. Stat. Softw.*, 2012, **49**, 1–22.

52 B. S. Al-Saadi, A. R. Ibrahim, J. Husband, A. H. Ismail, Y. Baqi and O. K. Abou-Zied, *Phys. Chem. Chem. Phys.*, 2024, **26**, 12844–12851.

53 P. Verma, R. Mathew, N. Dhiman, P. K. Mitra and Y. A. Lakshmanna, *Phys. Chem. Chem. Phys.*, 2025, **27**, 7716–7727.

54 J. Jia, X. Wu, X. Zhang, Y. Wang, J. Yang, Y. Fang and Y. Song, *Phys. Chem. Chem. Phys.*, 2022, **24**, 955–965.

55 H. Zhu, M. Li, J. Hu, X. Wang, J. Jie, Q. Guo, C. Chen and A. Xia, *Sci. Rep.*, 2016, **6**, 24313.

56 M. Jia, X. Ma, L. Yan, H. Wang, Q. Guo, X. Wang, Y. Wang, X. Zhan and A. Xia, *J. Phys. Chem. A*, 2010, **114**, 7345–7352.

57 B. Carlotti, E. Benassi, A. Spalletti, C. G. Fortuna, F. Elisei and V. Barone, *Phys. Chem. Chem. Phys.*, 2014, **16**, 13984–13994.

58 G. Kedawat, I. Sharma, K. Nagpal, M. Kumar, G. Gupta and B. K. Gupta, *ACS Omega*, 2019, **4**, 12626–12631.

59 S. Link and M. A. El-Sayed, *J. Phys. Chem. B*, 1999, **103**, 8410–8426.

60 M. Gordel-Wójcik, R. Kołkowski, M. Nyk and M. Samoć, *ACS Appl. Mater. Interfaces*, 2025, **17**, 28484–28494.

61 V. Pustovalov, *Nanotechnol. Precis. Eng.*, 2025, **7**, 015001.